

EARLY ONLINE RELEASE

This is a PDF of a manuscript that has been peer-reviewed and accepted for publication. As the article has not yet been formatted, copy edited or proofread, the final published version may be different from the early online release.

This pre-publication manuscript may be downloaded, distributed and used under the provisions of the Creative Commons Attribution 4.0 International (CC BY 4.0) license. It may be cited using the DOI below.

The DOI for this manuscript is

DOI:10.2151/jmsj.2023-002

J-STAGE Advance published date: October 7th, 2022

The final manuscript after publication will replace the preliminary version at the above DOI once it is available.

1
2
3
4
5
6
7
8
9
10
11
12
13
14
15
16
17
18
19
20
21
22
23
24
25
26
27
28
29

Two Types of Wintertime Teleconnection Patterns over the Western North Pacific associated with Regionally Different Heating Anomalies

Masaya KURAMOCHI¹

*Graduate School of Science and Technology
University of Tsukuba, Tsukuba, Japan*

and

Hiroaki UEDA

*Faculty of Life and Environmental Sciences
University of Tsukuba, Tsukuba, Japan*

First draft: March 18, 2022
1st revision: July 6, 2022
2nd revision: September 6, 2022

1) Corresponding author: Masaya Kuramochi, Graduate School of Science and Technology, University of Tsukuba, 1-1-1 Tennodai, Tsukuba, Ibaraki, 305-8572 JAPAN
Email: kuramochi.masaya.sp@alumni.tsukuba.ac.jp
Tel: +81-29-853-5692

Abstract

The turnabout of air temperature anomalies over East Asia between the first and second halves of winter 2020/21 was examined from a teleconnection perspective with regionally different convective heating anomalies over the Indo-western Pacific sector. In the first half of winter 2020/21, the air temperature over East Asia was lower than normal, accompanied by a pair of anticyclonic and cyclonic anomalies in the upper troposphere southeast of the Tibetan Plateau and north of Japan, respectively. This dipole pattern is newly referred to as Southeast Asia–Japan (SAJ) pattern in this study, indicating the propagation of Rossby waves caused by enhanced tropical convection over the eastern Indian Ocean toward the South China Sea. In the second half of winter 2020/21, the enhanced convection shifted eastward to the Philippine Sea. The subsequent anticyclonic anomaly changed its position to the south of Japan, which was similar to the western Pacific (WP)-like teleconnection pattern, causing warmer conditions over East Asia. The composite analysis indicated that the anomalous anticyclone over the southeastern Tibetan Plateau corresponding to the SAJ pattern emerged simultaneously with intensification of convection over the South China Sea. Half of the cases of the WP-like pattern have been accompanied by enhanced convection over the Philippine Sea. The different circulation patterns were reproduced by prescribing the heat source over the South China Sea and Philippine Sea to the linear baroclinic model. Moreover, the vorticity budget analysis suggested that the presence of upper-tropospheric convergence of winds

50 to the southeast of the Tibetan Plateau seen in the climatology is conceivable for the in
51 situ localized anomalous circulation constituting the SAJ pattern due to vortex stretching
52 effects.

53

54 **Keywords** teleconnection; heat-induced atmospheric response; East Asian winter
55 monsoon; climate variability; vorticity budget

56

57 **1. Introduction**

58 The western Pacific (WP) pattern is a tropospheric teleconnection pattern in boreal winter,
59 which consists of a north–south dipole of height anomalies over the Kamchatka Peninsula
60 and the western subtropical North Pacific (Wallace and Gutzler 1981). The WP pattern
61 influences climate variability over East Asia (Takaya and Nakamura 2013; Park and Ahn
62 2016; Shiozaki et al. 2021; Shiozaki and Enomoto 2021) and the frequency of blocking
63 associated with Rossby wave breaking (Pavan et al. 2000; Rivière 2010). The monthly or
64 seasonal geopotential height anomaly corresponding to the WP pattern was investigated in
65 association with the El Niño–Southern Oscillation (ENSO). Observational evidence and
66 numerical studies have shown that a positive (negative) WP pattern tends to appear more
67 frequently when El Niño (La Niña) occurs (Horel and Wallace 1981; Ferranti et al. 1994;
68 Trenberth et al. 1998; Koide and Kodera 1999; Dai and Tan 2019). However, a positive WP
69 pattern has been observed not only in El Niño months but also in La Niña months (Tanaka
70 et al. 2016). In this study, the positive WP pattern is defined as when the southern part of
71 the dipole is high and the northern part is low. It has also been indicated that the emergence
72 of the WP pattern, linked to ENSO, may be affected by anomalous circulation over the
73 Eurasian continent during early winter (Kodera 1998). Tanaka et al. (2016) showed that the
74 WP pattern could be sustained by baroclinic energy conversion associated with heat
75 transport by energetic analysis based on monthly mean data and concluded that the WP
76 pattern could be maintained even without external forcing.

77 As for the interannual variability of the East Asian winter monsoon, especially in air
78 temperature over the Far East, a more effective north–south dipole pattern could shift slightly
79 westward compared with that of the canonical WP pattern (Takaya and Nakamura 2013).
80 Takaya and Nakamura (2013) referred to the upper-tropospheric pattern as the “WP-like”
81 pattern. These facts indicate that WP-like dipole patterns can appear at slightly different
82 positions from the action center shown by Wallace and Gutzler (1981), and its locality is an
83 important factor influencing climate variability over East Asia.

84 The variability of the East Asian winter monsoon is closely related to the modulation of
85 tropical convective activity over the Indo-western Pacific sector (Hong and Li 2009; Sakai
86 and Kawamura 2009; Ueda et al. 2015; Abdillah et al. 2017; Kuramochi et al. 2021). They
87 showed a southwest–northeast dipole pattern (or wave train) of circulation anomalies from
88 southern China to Japan in the upper troposphere caused by anomalous diabatic heating
89 around the Maritime Continent, which is a dominant spatial mode over Asia during the winter
90 season (Zheng et al. 2013). For convenience, hereafter, we refer the southwest–northeast
91 dipole pattern as the “southeast Asia–Japan (SAJ) pattern.” The SAJ pattern, especially in
92 the southwestern portion of the dipole, is salient in the upper troposphere (~300–200 hPa);
93 however, becomes obscure in the mid-troposphere (~500 hPa) (Ueda et al. 2015; Abdillah
94 et al. 2017). This vertical structure seems to be consistent with the baroclinic mode of the
95 heat-induced Rossby wave response (Gill 1980; Wu et al. 2015a, 2015b) and differs from
96 the characteristics of the WP pattern.

97 The winter climate variability over East Asia is affected by both WP(-like) and SAJ
98 patterns. The spatial distributions of the two types of dipole patterns differ, indicating
99 dynamically different excitation mechanisms. Our main objective is to assess the structure
100 and dynamics of the two teleconnection patterns.

101 In this study, we first focus on a change in air temperature from cold to warm over East
102 Asia during the winter season in 2020/21, linked with the modulation of atmospheric
103 circulation fields (Japan Meteorological Agency [JMA] 2021a, 2021b). Figure 1a shows the
104 time series of the air temperature anomaly at 850 hPa averaged over East Asia [25°–45°N,
105 100°–140°E] from December 1, 2020, to February 28, 2021. The air temperature anomaly
106 changed from negative to positive around January 14, 2021. In this study, we defined two
107 periods: the colder period (Period 1: from December 13, 2020, to January 11, 2021) and the
108 warmer period (Period 2: from January 23, 2021, to February 21, 2021). The anomalous
109 coldness in Period 1 was associated with the SAJ pattern, while the warmth in Period 2 was
110 the WP-like pattern, as discussed below in Section 3. The present study examines the
111 difference between these two periods and the factor of air temperature transition from the
112 teleconnection perspective; moreover, the inherent physical mechanism involved in the SAJ
113 and WP(-like) patterns anchored with anomalous convection over the tropical western
114 Pacific is investigated by comparing their differences.

115

116 **2. Data and methods**

117 The data used in this study were monthly mean and 6-hourly data from the Japanese 55-
118 year Reanalysis dataset (JRA-55) with a horizontal resolution of 1.25° and 37 pressure
119 levels (Kobayashi et al. 2015), daily data from the National Oceanic and Atmospheric
120 Administration (NOAA) Interpolated Outgoing Longwave Radiation (OLR) dataset with a
121 horizontal resolution of 2.5° (Liebmann and Smith 1996), and monthly mean sea surface
122 temperature (SST) data from the Centennial in Observation-Based Estimate-SST (COBE-
123 SST; Ishii et al. 2005) for December–February (DJF) during the 47 years from 1974/75 to
124 2020/21. To examine daily oceanic conditions, the NOAA Daily Optimum Interpolation SST
125 (OISST; Reynolds et al. 2007) from 1981 to 2021 was also utilized. To abstract high-
126 frequency components, an appropriate running mean was applied to the 6-hourly and daily
127 data. In this study, climatological mean states were defined as the 47-year average during
128 the study period (41-year average only for the OISST), and anomalies are defined as
129 deviations from the climatological mean states.

130 The propagation of stationary Rossby wave packets was analyzed using the quasi-
131 geostrophic wave-activity flux defined by Takaya and Nakamura (2001). The horizontal
132 component of the flux \mathbf{W} is defined as follows:

$$133 \quad \mathbf{W} = \frac{p}{2\sqrt{\bar{u}^2 + \bar{v}^2}} \left(\bar{u}(\psi_x'^2 - \psi'\psi'_{xx}) + \bar{v}(\psi_x'\psi_y' - \psi'\psi'_{xy}) \right), \quad (1)$$

134 where the overbar and prime denote the climatological state and anomaly, respectively, u
135 is the zonal wind, v is the meridional wind, ψ is the geostrophic streamfunction, and $p =$
136 (pressure/1000hPa). The subscripts x and y denote partial derivatives concerning

137 longitude and latitude, respectively.

138 To assess the role of tropical convection in the excitation and maintenance of circulation
139 patterns, vorticity budget analysis was conducted. The linearized barotropic vorticity
140 equation is written as follows (Sardeshmukh and Hoskins 1988):

$$141 \quad \frac{\partial \zeta'}{\partial t} = S' - \bar{\mathbf{v}}_{\psi} \cdot \nabla \zeta' - \mathbf{v}'_{\psi} \cdot \nabla \bar{\zeta} + R', \quad (2)$$

142 where ζ is the absolute vorticity, \mathbf{v}_{ψ} is the rotational wind vector, and R' is the residual
143 term, including the frictional term. S' is the so-called Rossby wave source (RWS) and is
144 defined as follows:

$$145 \quad S' = -\nabla \cdot (\mathbf{v}'_{\chi} \bar{\zeta}) - \nabla \cdot (\bar{\mathbf{v}}_{\chi} \zeta')$$
$$146 \quad = -\bar{\zeta} D' - \mathbf{v}'_{\chi} \cdot \nabla \bar{\zeta} - \zeta' \bar{D} - \bar{\mathbf{v}}_{\chi} \cdot \nabla \zeta', \quad (3)$$

147 where \mathbf{v}_{χ} is the divergent wind vector and $D = \nabla \cdot \mathbf{v}_{\chi}$ is its divergence. The relatively small
148 twisting and vertical advection terms were neglected. Because the second and third terms
149 on the right-hand side of Eq. (2) are related to rotational winds (rotational terms), they
150 represent wave propagation rather than wave source. Perturbation RWS is the convergence
151 of the linearized vorticity flux associated only with the divergent wind component. The first
152 term of Eq. (3) is the vorticity generation by anomalous horizontal divergence (anomalous
153 divergence term; S_1), and the second term is the advection of climatological vorticity by
154 anomalous divergent wind (anomalous advection term; S_2). The third and fourth terms
155 represent the evolution of vorticity perturbation due to climatological divergence
156 (climatological divergence term; S_3) and advection of anomalous vorticity by climatological

157 divergent wind (climatological advection term; S_4), respectively. The S_3 term amplifies
158 perturbations in regions where climatological winds converge ($\bar{D} < 0$) and damps
159 perturbations in regions where they diverge ($\bar{D} > 0$).

160 To verify the linear response to tropical diabatic heating, we used the linear baroclinic
161 model (LBM; Watanabe and Kimoto 2000). The LBM is a spectral model based on linearized
162 primitive equations and has 20 sigma levels with a horizontal resolution of T42. The model
163 employed del-forth horizontal diffusion, Rayleigh friction, and Newtonian thermal damping.
164 The e-folding decay time of the diffusion coefficient was set to 4 h. The damping coefficient
165 was set at two days for the lowest three levels, one day for the uppermost two levels, and
166 30 days elsewhere. The LBM was forced with externally imposed heating and time-
167 integrated to a steady state. The details of the experimental settings, including the
168 prescribed heating and background states, are mentioned in Section 4.2.

169

170 **3. Turnabout of air temperature and two types of teleconnection patterns in winter**

171 **2020/21**

172 *3.1 Zonal shift of circulation anomaly linked with anomalous tropical convection*

173 The first half of the winter of 2020/21 was colder than normal over East Asia. In contrast,
174 the latter half became warmer (Fig. 1a). Figures 1b and 1c show circulation and temperature
175 anomalies in the lower troposphere during the two defined periods. In Period 1, East Asia
176 and Siberia were colder than the climatological state, and the anomalous northwesterly flow

177 was indicative of intensification of the East Asian winter monsoon, together with the
178 deepened northern part of the Aleutian low. However, in Period 2, the cold air remained alive
179 over northern Eurasia; nevertheless, the air temperature over East Asia became warmer
180 than normal, which is associated with an anticyclonic circulation anomaly extending to Japan
181 from the North Pacific. The remote influence of tropical modulations is suggested explaining
182 the variation in air temperature anomalies.

183 One noteworthy feature of this winter was the continued La Niña condition, which can be
184 seen from the negative values of the Niño-3.4 SST anomaly (Fig. 1a). Niño-3.4, a widely
185 used index of ENSO, is defined as the averaged SST anomaly over the equatorial eastern
186 Pacific [5°S–5°N, 170°E–120°W] (Trenberth 1997). The positive values of the SST anomaly
187 in the Niño-WP [0°–10°N, 130°–150°E] (Hoell and Funk 2013) also exhibit La Niña
188 conditions (Fig. 1a), which set up an easy-to-enhance environment for convection over the
189 tropical western Pacific owing to the in situ anomalous warm SST. In a La Niña winter, the
190 East Asian winter monsoon tends to be stronger than normal (Wang et al. 2000; Zhou and
191 Wu 2010), although the air temperature over East Asia was warmer in the latter half of winter
192 2020/21. This inconsistency suggests that intraseasonal variability contributed to the
193 dramatic turnabout of temperature anomalies, rather than prolonged SST anomalies.

194 The anomalies of the upper-tropospheric circulation and OLR, together with the wave-
195 activity flux in the two periods, are shown in Figures 2a and 2b. The negative values of the
196 OLR anomaly in the tropics correspond to the enhancement of tropical convection. In Period

197 1, anticyclonic and cyclonic circulation anomalies emerged over the region from the
198 southeast of the Tibetan Plateau to southern China and over the northern part of Japan,
199 respectively, exhibiting a southwest–northeast dipole pattern. The northeastward wave-
200 activity flux emanating from the dipole’s southwestern anomaly indicates the propagation of
201 stationary Rossby waves. In addition, southeastward propagation from the Caspian Sea to
202 the northern part of India was confirmed. Concurrently, in the tropics, enhanced convection
203 was discernible over the South China Sea toward the eastern Indian Ocean. These
204 modulated atmospheric fields are responsible for the colder-than-normal conditions and
205 heavy snowfall in Japan during winter 2020/21 (JMA 2021a) and are almost consistent with
206 the features of the SAJ pattern as well as the typical mode of the cold East Asian winter
207 (Hong and Li 2009; Sakai and Kawamura 2009; Ueda et al. 2015; Abdillah et al. 2017;
208 Shiozaki and Enomoto 2021). Corresponding to the enhanced equatorial convection,
209 anomalous divergent flows occurred in the upper troposphere over the Philippines and
210 southern India (Fig. 2c).

211 In Period 2, the location of the anticyclonic anomaly around 30°N shifted eastward,
212 causing anomalously warm conditions to associate with attenuated cold air outbreaks (Fig.
213 1). The meridional dipole pattern across the Japanese islands resembles the WP pattern
214 (Fig. 2b), however, this pattern is referred to as the “WP-like” pattern in the present study
215 because the southern anomaly of the dipole is located westward compared to the action
216 center of the canonical WP pattern (160°E). Notably, the northern cyclonic anomaly was not

217 as clear as the southern anticyclonic anomaly. We could not find any noticeable wave packet
218 propagation from upstream, which seems consistent with the WP-like blocking analyzed by
219 Takaya and Nakamura (2005). The center of the enhanced convection was located from the
220 Philippine Sea to Indonesia, and convective activity over the South China Sea toward the
221 eastern Indian Ocean had already decayed. This zonal shift of the anomalous convection
222 center on the intraseasonal timescale, such as the Madden-Julian oscillation (MJO: Madden
223 and Julian 1972), can also be confirmed from the time–longitude cross-section (Fig. 3). The
224 negative OLR anomaly persisted around 80° – 120° E from mid-December 2020 until January
225 2021 (Period 1), and around 120° – 150° E in February 2021 (Period 2). The MJO phase
226 transition induces different upper-tropospheric circulations through modulated divergent
227 fields (Cassou 2008; Seo and Son 2012). Thus, the anomalous divergence and its winds
228 (Figs. 2c and 2d) likely caused the different positions of the subtropical anticyclonic anomaly
229 of the dipole patterns between the two periods, which will be discussed in Subsection 3.2.

230

231 *3.2 Vorticity budget analysis in the first and second halves of winter 2020/21*

232 Figure 4 shows the climatological mean state of the upper troposphere over the western
233 North Pacific region. The strong westerly jet and northward positive meridional gradient of
234 absolute vorticity are the most important features in East Asia during winter (Fig. 4a).
235 Moreover, the southern Tibetan Plateau in the upper troposphere is a very intense
236 convergence area of winds associated with deep convection over the Indo-western Pacific

237 sector (Fig. 4b). These unique background states play essential roles in anomalous vorticity
238 generation in vorticity budget analysis.

239 The upper-tropospheric vorticity budget was determined based on the steady state of Eq.
240 (2), that is,

$$\begin{aligned} 241 \quad 0 &\equiv S' + (\text{rotational terms}) + R' \\ 242 \quad &= S_1 + S_2 + S_3 + S_4 + (\text{rotational terms}) + R'. \quad (4) \end{aligned}$$

243 The distributions of the RWS and rotational terms in the upper troposphere based on the
244 time mean data in Periods 1 and 2 are shown in Figures 5 and 6, respectively. Vorticity fields
245 were applied weak horizontal smoothing. Emphasis is placed on the anomalous subtropical
246 anticyclone that constitutes the southern part of the dipole pattern in each period. In Period
247 1, negative vorticity (anticyclonic) anomaly was evident over the southeastern Tibetan
248 Plateau toward southern China (contours), which corresponds to the anomalous subtropical
249 anticyclone (Fig. 2a). As shown in Figure 5a, a negative RWS was distributed over the
250 western and northern parts of the anticyclonic vorticity anomaly. The negative RWS to the
251 upstream of the anomalous anticyclone along the subtropical jet (25° – 35° N) was almost
252 balanced by the positive vorticity tendency seen in the rotational term (Fig. 5b). In the
253 presence of strong westerlies, wave trains of perturbation cyclonic and anticyclonic
254 circulations are responsible for the positive vorticity advection upstream of the anticyclonic
255 anomaly and downstream of the cyclonic anomaly owing to the mean flow, which was larger
256 than the vorticity advection by anomalous rotational wind corresponding to the β term

257 between the rotational terms in Eq. (2) (Fig. S1). The RWS (Fig. 5a) primarily arises from
258 the stretching effect of anomalous divergence (S_1 ; Fig. 5c), and the advection term by
259 anomalous divergent wind (S_2 ; Fig. 5d) also contributes to negative vorticity generation over
260 the western portion of the anticyclonic vorticity anomaly by crossing the climatological jet
261 northward. Here, note that the RWS, especially S_1 , includes not only the effect of
262 extratropical convergence of upper-tropospheric wind induced by enhanced tropical
263 convection (Held and Kang 1987; Rasmusson and Mo 1993) but also the vorticity tendency
264 associated with the stationary Rossby wave trains themselves to maintain their structure in
265 the vertically sheared westerlies, which may be understood by quasi-geostrophic dynamics
266 (Qin and Robinson 1993; Sekizawa et al. 2021). The latter refers to the vortex stretching
267 effect balancing with the vorticity advection by mean flow under strong westerlies, as
268 mentioned above (Lau 1979; Honda et al. 1999; Chen 2005). It is widely accepted that the
269 advection of mean vorticity by upper-tropospheric divergent flow associated with anomalous
270 equatorial heating (i.e., S_2) induces anticyclonic circulation (Sardeshmukh and Hoskins
271 1988; Jin and Hoskins 1995), which is an important factor in the generation of anomalous
272 circulations also on intraseasonal timescales (Mori and Watanabe 2008; Seo and Lee 2017).

273 The climatological divergence term (S_3 ; Fig. 5e) is found over the center of the
274 anticyclonic vorticity anomaly, which is related to vortex stretching due to the intense
275 background convergence over the southern Tibetan Plateau (Fig. 4b) acting on the
276 anomalous vorticity. S_3 seems to counterbalance S_1 over the center of the anomalous

277 vorticity rather than their nodes, canceling out the mutual stretching effect (Fig. 5c) because
278 S_3 cannot balance with the rotational terms. The contribution of S_3 may explain the localized
279 anomalous circulation over the southeastern Tibetan Plateau toward southern China when
280 considering a steady state. Indeed, the climatological convergence region can produce a
281 vorticity source on the perturbation vorticity (Sardeshmukh and Hoskins 1988; Trenberth et
282 al. 1998), and its importance has been confirmed by numerical studies (Grimm and Silva
283 1995a, 1995b). The climatological advection term (S_4 ; Fig. 5f) dominated the southeastern
284 part of the RWS, particularly the positive values around the anomalous anticyclone (Fig. 5a).
285 This term acts to advect the circulation anomaly poleward.

286 During Period 2 (Fig. 6), the negative vorticity anomaly corresponding to the southern
287 part of the WP-like pattern was located south of Japan. Again, we focused on subtropical
288 anticyclonic anomalies. The RWS (Fig. 6a) counterbalanced the rotational terms (Fig. 6b)
289 over the northwest of the anticyclonic vorticity anomaly. The anomalous divergence (S_1 ; Fig.
290 6c) and advection terms (S_2 ; Fig. 6d) were the main components of the RWS (Fig. 6a). While,
291 the contributions of climatological divergence and its flow (S_3 and S_4) were small around the
292 anomalous anticyclonic vorticity (Figs. 6e and 6f). The rotational terms were predominant in
293 the southeastern portion of the vorticity anomaly owing to the strong westerly winds, which
294 may have been compensated by the residuals.

295

296 **4. Statistical analyses and numerical experiments**

297 *4.1 Composite analysis of the SAJ and WP-like patterns*

298 Composite analysis was performed to obtain and compare the statistical characteristics
299 of the SAJ and WP-like patterns. Here, we define two indices that represent the dipole
300 patterns to extract and composite the teleconnection patterns. The index of the SAJ pattern
301 is defined as the deviation of the normalized anomalous geopotential height at 250 hPa
302 (Z250) averaged from the southeast of the Tibetan Plateau to southern China [20°–30°N,
303 80°–120°E] and the corresponding anomaly over northern Japan [40°–50°N, 130°–160°E],
304 with reference to Ueda et al. (2015). The index of the WP-like pattern is defined as the
305 deviation of the normalized Z250 anomaly averaged over the western North Pacific [20°–
306 40°N, 130°–160°E] and over the Sea of Okhotsk [45°–65°N, 130°–160°E]. Thus, the
307 northern-low southern-high height anomaly patterns correspond to positive phases. These
308 two indices were calculated from the monthly mean data, and normalization was based on
309 the standard deviation of each month. The wintertime months for which each index
310 exceeded +1 (–1) standard deviation for the 141 (DJF × 47 years) calendar months were
311 used as those for the positive (negative) phase of the dipole patterns. For the composite of
312 the WP-like pattern, additional filtering was applied using the OLR anomaly averaged over
313 the domain of 5°S–10°N, 120°–160°E, to determine whether convection was enhanced over
314 the tropical western Pacific. In this analysis, we focused on the positive (negative) WP-like
315 pattern accompanied by enhanced (suppressed) convection over the tropical western
316 Pacific, such as in the case of winter 2020/21. Based on these criteria, 20 months (21

317 months) were selected as the positive (negative) SAJ pattern months and 11 months (9
318 months) were selected as the positive (negative) phase of the WP-like pattern accompanied
319 by a negative (positive) OLR anomaly (Table 1). Interestingly, the months of the WP-like
320 pattern were divided by almost half by OLR filtering.

321 Figure 7 shows the composite anomalies of geopotential height, OLR, and air
322 temperature between the positive and negative phases based on the monthly mean data.
323 The positive phase of the SAJ pattern was significantly correlated with enhanced convection
324 over the Maritime Continent, and its maximum was discernible over the South China Sea
325 (Fig. 7a). The anomalous northwesterly flow in the lower troposphere indicates an intensified
326 East Asian winter monsoon, causing colder-than-normal conditions over the Far East (Fig.
327 7c). These features bear a considerable resemblance to those described in previous studies;
328 however, the positions of the anomalous convection and northern circulation of the dipole in
329 our results differ slightly from their results based on the DJF mean. When the SAJ index is
330 applied to the DJF mean data (Fig. S2), the anomalous circulation was almost the same as
331 that indicated previously (Zheng et al. 2013; Ueda et al. 2015; Abdillah et al. 2017).

332 The composited Z250 anomaly based on the WP-like index filtered with the OLR anomaly
333 (Fig. 7b) is more zonally elongated than that of winter 2020/21 (Fig. 2b) and resembles the
334 canonical WP pattern. The defined WP-like index is significantly correlated with the WP
335 index defined at 500 hPa by Wallace and Gutzler (1981) ($r = -0.89$); note that the sign is the
336 opposite. The weak baroclinic structure of the southern pole of the dipole as a southward tilt

337 with height (Figs. 7b and 7d) was consistent with that proposed by Tanaka et al. (2016).
338 Anomalous convective activity was distributed only around the Philippine Sea, and no
339 modulated convection was confirmed over the eastern Indian Ocean and the Malay
340 Peninsula (Fig. 7b), which may be important when considering the effective wave source.
341 Cold anomalies were evident around the Sea of Okhotsk to the far eastern Siberia, and
342 oppositely air temperatures over western Japan tended to be warmer, associated with
343 anomalous southeasterly winds (Fig. 7d).

344 The correlation coefficients between the Z250 and ENSO indices are listed in Table 2.
345 The SAJ pattern is correlated with ENSO, especially tropical western Pacific SST. These
346 correlations became more potent on the seasonal (DJF) timescale. Indeed, the upper-
347 tropospheric height anomaly over southern China, an action center of the SAJ pattern, is
348 recognizable in the response to the wintertime ENSO (Wang et al. 2000; Shiozaki and
349 Enomoto 2021). A recent study showed that SAJ-type anomalies tend to appear in the first
350 winter of the multi-year La Niña, which is more influential on the East Asian air temperature
351 than the second winter (Nishihira and Sugimoto 2022). In contrast, the WP-like index (not
352 filtered) showed no significant correlation with ENSO.

353

354 *4.2 Vorticity budget in the composite anomalies*

355 In Section 3.2, it was implied that the SAJ and WP-like patterns were attributed to the
356 different vorticity balances. We also performed the vorticity budget analysis for the

357 composited anomalies. Figure 8a shows a comparison of the vorticity tendency terms in Eq.
358 (4), averaged over the center and upstream nodes of the subtropical anticyclonic anomaly
359 in the positive phase of the SAJ pattern. At the center of the anomaly (heavy blue bars), the
360 S_3 term counterbalances the S_1 term, which can be written as

361
$$S_1 + S_3 = -\bar{\zeta}D' - \zeta'\bar{D} \approx 0. \quad (5)$$

362 This balance is consistent with the case of winter 2020/21 mentioned in Section 3.2 (Fig. 5)
363 and can be identified as important dynamics of the SAJ pattern. The positive S_1 is due to
364 the anomalous convergence of winds ($D' < 0$) induced by the enhanced convection over the
365 Maritime Continent (Fig. 7a). The climatological convergence area ($\bar{D} < 0$) requires
366 anomalous negative vorticity to balance the positive vorticity tendency of the stationary eddy.
367 In contrast, the RWS term (S') is balanced by the rotational terms (rot.) at the upstream
368 nodes (light blue bars). The positive rotational terms represent the dominant vorticity
369 advection from the upstream cyclonic anomaly by climatological mean flow, as shown in
370 Figures 5b and S1a. Although the negative S' term arises from S_2 and S_3 in the composite
371 analysis (Fig. 8a), S_1 may also theoretically contribute to the balance with the rotational
372 terms (e.g., Honda et al. 1999), as seen in the case of winter 2020/21 (Fig. 5c). The inherent
373 vorticity budget of the anticyclonic perturbation over the southeast of the Tibetan Plateau is
374 schematically summarized in Figure 8b.

375 Figure 9 shows the vorticity budget of the positive WP-like pattern accompanied by
376 enhanced convection over the tropical western Pacific. Here, emphasis is placed on the

377 center of the subtropical eddy, however, the composited vorticity anomaly is zonally
378 elongated and its center is unclear (upper panel of Fig. 9). The vorticity budget shows the
379 predominant contributions of the rotational, S_1 , and residual terms. The intense jet stream is
380 responsible for the large magnitude of the rotational terms, and S_1 attempts to balance them.
381 The residual term may be associated with relatively short-period eddies. Indeed, Tanaka et
382 al. (2016) and Sekizawa et al. (2021) indicate the importance of feedback forcing by
383 submonthly and transient eddies in the maintenance of the WP(-like) pattern. Similar to the
384 2020/21 case (Fig. 6), the relatively small negative S_2 term represents advection by
385 anomalous divergent winds induced by the enhanced convection over the Philippine Sea
386 (Fig. 7b). The S_3 term is almost zero because of the in situ non-divergence of the background
387 winds (Fig. 4b), which differs from the balance of the SAJ pattern (Fig. 8).

388

389 *4.3 Sensitivity experiments using the LBM*

390 The previous sections indicated that regionally different heating anomalies in the tropics
391 could be responsible for the two types of teleconnection patterns. To confirm this hypothesis,
392 sensitivity experiments for tropical convective heating were conducted using the LBM
393 described by Watanabe and Kimoto (2000). We performed two experiments that differed
394 only in the positions of the prescribed heating: one was over the South China Sea (the center
395 was at 8°N, 110°E), and the other was over the Philippine Sea (the center was at 10°N,
396 135°E), which corresponded to the composited OLR peaks (Figs. 7a and 7b). The imposed

397 heating exhibited an oval shape, with its heating maxima at its center (as shown in Fig. 10).
398 The heating also had a vertical structure that peaked at $\sigma = 0.45$, where the maximum
399 heating rate was approximately $+1.0 \text{ K day}^{-1}$, which imitated the vertical profile of the
400 composite anomalous diabatic heating calculated as the residual of the thermodynamic
401 equations (Yanai et al. 1973). The background atmospheric state was DJF climatology
402 derived from JRA-55, and the response on day 15 is shown when the model reached a
403 quasi-steady state.

404 Figure 10 shows the steady response of the upper troposphere to imposed tropical
405 heating. The response to South China Sea heating roughly reproduced the wave train of
406 height anomalies corresponding to the SAJ pattern (Fig. 10a). The anomalous anticyclone
407 north of the Indian subcontinent could be interpreted as the western margins of the Matsuno-
408 Gill type heat-induced atmospheric response (Matsuno 1966; Gill 1980) when the vertical
409 gradient of the heating is considered (Wu et al. 2015a). It should be noted here that the
410 anticyclone seen in the geopotential height field locates slightly westward in comparison with
411 the reanalysis (Fig. 7a). This may be partly due to lack of extratropical forcing as well as a
412 model bias (Tseng et al. 2020). The vorticity balance indicated in the present study (Figs. 5
413 and 8) is inherently caused by the combined effect of climatological mean flows and external
414 forcing. Hence, the SAJ-like steady perturbation vorticity tends to emerge over the region of
415 convergence area of winds and under the subtropical jet in the climatological mean (Fig. 4).
416 As for the atmospheric response to heating over the Philippine Sea (Fig. 10b), the positive

417 height anomaly is recognizable to the south of Japan. Its position is the same as that of the
418 southern part of the WP-like pattern. Note that the northern cyclonic anomaly of the WP(-
419 like) pattern was not clearly reproduced.

420 The noteworthy difference between the results of the two experiments is the subsequent
421 steady positions of the generated anticyclonic anomalies, although the imposed heat
422 sources were only 25° longitude apart from each other. If we pay attention to its time
423 evolution, after the anticyclone was generated over the northwest of the heat source as a
424 first response in the South China Sea experiment, it shifted northward and consequently
425 stayed north of the Indian subcontinent (Figs. 10a and S3). Similarly, the anticyclonic
426 anomaly seen in the results of the Philippine Sea experiment was also first generated
427 northwest of the heat source, after which, however, it moved northeastward and stayed north
428 of the heat source (Figs. 10b and S3). These meridional shifts of the anomalous circulations
429 may be explained by the effects of the background divergent wind. As mentioned in the RWS
430 analysis, the climatological divergent flow advects the anomalous vorticity poleward in the
431 subtropics (S₄, Figs. 5 and 6). Using numerical experiments, Sekizawa et al. (2021)
432 demonstrated that poleward vorticity advection is an essential role of the background
433 divergent wind in the establishment of the subtropical anomalous anticyclone. Based on this
434 idea, the additional eastward shift of the anomalous anticyclone of the WP(-like) pattern can
435 be attributed to advection by the background jet core represented by the rotational terms in
436 Eq. (2). Thus, it is suggested that the unique background winds, as well as the regionally

437 different anomalous heating, are responsible for the significantly different steady locations
438 of the anomalous anticyclones and the related teleconnection patterns.

439

440 **5. Discussion**

441 *5.1 Significance of the SAJ pattern*

442 The wave train pattern referred to as the SAJ pattern in this study had been indicated in
443 association with East Asian climate variability during winter in previous research. To confirm
444 its significance for the interannual variability of atmospheric circulation in Asia, we performed
445 an empirical orthogonal function (EOF) analysis to the seasonal (DJF) mean Z250 over the
446 domain of 10°S–70°N, 10°–180°E, including the tropical and extratropical upstream regions.
447 The spatial distributions of the anomalies of streamfunction and OLR corresponding to the
448 first (EOF1) and second EOF modes (EOF2) are illustrated in Figure 11. EOF1 explained
449 approximately 23.4% of the total variance for the period 1974/75–2020/21, while EOF2
450 explained approximately 20.0%. The anomalies of upper-tropospheric circulation and
451 convective activity associated with EOF1 resemble those based on the SAJ index (Figs. 7a,
452 7c, and S2). The correlation coefficient between the seasonal mean SAJ index and EOF1 is
453 0.74. Furthermore, EOF1 is similar to the height anomalies associated with the dominant
454 variation of the East Asian winter monsoon (Sakai and Kawamura 2009) and rainfall over
455 the Indo-western Pacific sector (Zheng et al. 2013). In addition, we noticed a similar anomaly
456 around southern China in EOF2 (Fig. 11b) although its amplitude is smaller than that of

457 EOF1. These results imply that the region from the southeast of the Tibetan Plateau to
458 southern China is an important fluctuation center of the upper-tropospheric circulation from
459 the teleconnection perspective, which may be attributed to the intense background
460 convergence of winds as well as the climatological subtropical jet (Figs. 4, 5, and 8).

461 It should be pointed out that the circulation anomalies around Japan of EOF1 and EOF2
462 differ remarkably from each other (Figs. 11a and 11b), despite the similar anomaly of
463 convective activity around the Maritime Continent and the resultant anomalous circulation
464 over southern China (Figs. 11c and 11d). The wave train northeastward from the Maritime
465 Continent via Japan to the Kamchatka Peninsula seen in EOF2 (Fig. 11b) can be identified
466 as a WP(-like) pattern accompanied by anomalous circulation over southern China rather
467 than the SAJ pattern. The circulation anomaly over southern China can form the WP(-like)
468 pattern by acting as a vorticity source for the emanation of northeastward-propagating
469 stationary waves. Indeed, the modulated circulation field of EOF2 bears a striking
470 resemblance to the geopotential height anomalies associated with variation in the Australian
471 summer monsoon (Sekizawa et al. 2021) and El Niño (Shiozaki et al. 2021), which were
472 reported to induce a circulation anomaly over southern China and the subsequent WP
473 pattern. The OLR anomaly of EOF2 consistently extended to the Southern Hemisphere (Fig.
474 11d) compared to that of EOF1.

475 An essential difference between EOF1 and EOF2 appears to be the wave train at higher
476 latitudes. In EOF1 (Fig. 11a), the wave train along the polar jet from northern Europe via

477 Siberia to Japan can be identified as the Eurasian (EU) pattern (Wallace and Gutzler 1981).
478 The EU pattern shares the anomalous circulation over Japan with the SAJ pattern. It is
479 suggested that this coherent amplification along the polar and subtropical jets is an important
480 factor in generating the different circulation anomalies over Japan compared with EOF2. To
481 assess the relationship between the wave propagation along the two main jet streams is
482 awaited, which are linked with the EU and SAJ patterns respectively.

483

484 *5.2 Relationship between the WP(-like) pattern and the tropical modulations*

485 As for the controversial issue regarding the WP pattern, its linkage with tropical variations
486 such as ENSO remains unsolved. As shown in Table 1, not all of the positive (negative) WP-
487 like patterns were caused by enhanced (suppressed) convection in the south. Thus, the
488 correlation with tropical modulations is unclear (Table 2). Nevertheless, it is still influential in
489 determining the phase of the WP pattern that is likely to be triggered (Tanaka et al. 2016;
490 Dai and Tan 2019). Our study provides a possible mechanism by which tropical modulation
491 directly induces the WP(-like) pattern by providing a wave source for the southern portion of
492 the dipole.

493 The anomalous circulation associated with EOF2 indicates another type of WP(-like)
494 pattern concurrent with the opposite convection anomaly, that is, the cyclonic anomaly of
495 the southern part of the dipole against the enhanced convection over the tropical western
496 Pacific (Figs. 11b and 11d). As mentioned in the preceding subsection, this WP(-like) pattern

497 is accompanied by an anticyclonic circulation anomaly over southern China and intensified
498 heating around the Maritime Continent. The anomalous circulation over southern China
499 could be an important factor in generating the WP(-like) anomaly (Sekizawa et al. 2021).
500 Thus, in the case of EOF2, the enhanced convection around the Maritime Continent might
501 indirectly induce the negative WP(-like) pattern through wave propagation. The relationship
502 between the phase of the WP(-like) pattern and convective activity over the tropical western
503 Pacific should be surveyed in greater detail in future studies.

504

505 **6. Summary**

506 In this study, the modulated atmospheric circulation associated with the turnabout of air
507 temperature anomalies over East Asia between the first and latter halves of the winter of
508 2020/21 was examined. In the colder-than-normal first half, a pair of anticyclonic and
509 cyclonic circulation anomalies appeared in the upper troposphere over the southeastern
510 Tibetan Plateau and northern Japan, respectively. This southwest–northeast dipole pattern
511 (referred to as the SAJ pattern in this study) was accompanied by enhanced convection over
512 the South China Sea toward the eastern Indian Ocean and the stationary Rossby wave
513 propagation along the subtropical jet. However, in the latter half of winter, the anticyclonic
514 anomaly in the subtropics shifted to the south of Japan, and the resultant meridional dipole
515 was identified as the WP-like pattern. It altered the cold airflow around East Asia, causing
516 warmer-than-normal conditions. Simultaneously, the center of the reinforced convection

517 shifted eastward to the Philippine Sea. The subsequent divergence and flow between the
518 two periods related to the intraseasonal eastward shift of convective activity induced
519 different anomalous vorticity fields in the upper troposphere, satisfying each vorticity balance.

520 Further analysis revealed the inherent spatial structures and dynamics of the two
521 teleconnection patterns. The composite analysis showed that the SAJ pattern significantly
522 influenced the East Asian winter monsoon, and the magnitude of the anomalous air
523 temperature around the Sea of Japan was larger than that of the WP-like pattern. The center
524 of the modulated convection emerged over the South China Sea when the SAJ pattern
525 appeared on the monthly timescale. The dynamical structures of the SAJ pattern, focusing
526 on the vorticity balance of the anticyclonic anomaly corresponding to the southwestern pole
527 of the dipole, are schematically shown in Figure 8b. Anomalous diabatic heating around the
528 Maritime Continent induces an anticyclonic anomaly in the upper troposphere southeast of
529 the Tibetan Plateau with the aid of climatological divergent winds advecting the anomalous
530 vorticity poleward (S_4). At the center of the anticyclonic eddy, the negative vorticity
531 perturbation on the climatological convergence of winds (S_3) counterbalances the
532 anomalous convergence associated with the enhanced convection (S_1). The negative
533 vorticity advection by anomalous divergent flows crossing the subtropical jet northward (S_2)
534 acts to compensate for the positive advection by the mean rotational winds (rot.), together
535 with anomalous divergence to maintain the wave train structure in the upstream nodes of
536 the eddy. The anticyclonic anomaly is responsible for the cyclonic anomaly around Japan

537 through the propagation of stationary Rossby waves. The vorticity budget suggests the
538 critical role of the background convergence of the winds over the southeast of the Tibetan
539 Plateau in the emergence and maintenance of the spatially phase-locked anomaly of the
540 SAJ pattern.

541 In contrast, half of the positive (negative) WP-like patterns were accompanied by
542 enhanced (suppressed) convection over the Philippine Sea, which could directly induce the
543 southern pole of the WP-like pattern. The dominant vorticity advection by the rotational winds
544 and residual terms played essential roles in the vorticity balance of the WP-like pattern. The
545 results of the LBM experiments support the regionally different heat sources and background
546 winds responsible for the two types of teleconnection patterns.

547 Although we attempted to understand the wintertime climate variability over East Asia in
548 relation to some teleconnection patterns, especially from the perspective of tropical forcing,
549 it is also necessary to investigate it from mid- and higher latitudes. Further studies focusing
550 on tropical–extratropical interactions are required to better understand the dynamics of
551 teleconnections and to improve seasonal forecasting.

552

553

Data Availability Statement

554 The JRA-55 and COBE-SST datasets are provided by JMA (https://jra.kishou.go.jp/JRA-55/index_en.html;
555 <https://ds.data.jma.go.jp/tcc/tcc/index.html>), the Interpolated OLR and
556 OISST datasets by NOAA PSL (<https://psl.noaa.gov/>). Documents and codes for the LBM

557 are available at [<https://ccsr.aori.u-tokyo.ac.jp/lbm/sub/lbm.html>].

558

559

Supplement

560 Supplement 1 shows spatial distributions of decomposed rotational terms in Eq. (2) and
561 the β term during Period 1. Supplement 2 shows Z250 anomaly associated with the DJF
562 mean SAJ index. Supplement 3 shows time evolution of upper-tropospheric circulation
563 anomalies in the LBM experiments.

564

565

Acknowledgments

566 The authors are grateful to Dr. Meiji Honda and Dr. Koutarou Takaya for their helpful
567 comments and discussion. We also thank Dr. Masaru Inatsu and the anonymous reviewers
568 for their constructive comments on the earlier version of this paper. This work was supported
569 by the Japan Society for the Promotion of Science (JSPS) Grants-in-Aid for Scientific
570 Research (KAKENHI), Grant Number 21H00626K, the industry-academia collaboration
571 project for the anomalous warm winter 2019/2020 of University of Tsukuba, and the Global
572 Environment Research Fund (4-2102) of the Ministry of the Environment, Japan.

573

574

References

575 Abdillah, M. R., Y. Kanno, and T. Iwasaki, 2017: Tropical–extratropical interactions
576 associated with East Asian cold air outbreaks. Part I: Interannual variability, *J. Climate*, **30**,

577 2989–3007.

578 Cassou, C., 2008: Intraseasonal interaction between the Madden–Julian oscillation and the
579 North Atlantic oscillation. *Nature*, **455**, 523–527.

580 Chen, T.-C., 2005: The structure and maintenance of stationary waves in the winter Northern
581 Hemisphere. *J. Atmos. Sci.*, **62**, 3637–3660.

582 Dai, Y., and B. Tan, 2019: Two types of the western Pacific pattern, their climate impacts,
583 and the ENSO modulations. *J. Climate*, **32**, 823–841.

584 Ferranti, L., F. Molteni, and T. N. Palmer, 1994: Impact of localized tropical and extratropical
585 SST anomalies in ensembles of seasonal GCM integrations. *Quart. J. Roy. Meteor. Soc.*,
586 **120**, 1613–1645.

587 Gill, A. E., 1980: Some simple solutions for heat-induced tropical circulation. *Quart. J. Roy.*
588 *Meteor. Soc.*, **106**, 447–462.

589 Grimm, A. M., and P. L. Silva Dias, 1995a: Use of barotropic models in the study of the
590 extratropical response to tropical heat sources. *J. Meteor. Soc. Japan*, **73**, 765–780.

591 Grimm, A. M., and P. L. Silva Dias, 1995b: Analysis of tropical extratropical interactions with
592 influence functions of a barotropic model. *J. Atmos. Sci.*, **52**, 3538–3555.

593 Held, I. M., and I.-S. Kang, 1987: Barotropic models of the extratropical response to El Niño.
594 *J. Atmos. Sci.*, **44**, 3576–3586.

595 Hoell, A., and C. Funk, 2013: The ENSO-related west Pacific sea surface temperature
596 gradient. *J. Climate*, **26**, 9545–9562.

597 Honda, M., K. Yamazaki, H. Nakamura, and K. Takeuchi, 1999: Dynamic and
598 thermodynamic characteristics of atmospheric response to anomalous sea-ice extent in
599 the Sea of Okhotsk. *J. Climate*, **12**, 3347–3358.

600 Hong, C-C., and T. Li, 2009: The extreme cold anomaly over Southeast Asia in February
601 2008: roles of ISO and ENSO. *J. Climate*, **22**, 3786–3801.

602 Horel, J. D., and J. M. Wallace, 1981: Planetary-scale atmospheric phenomena associated
603 with the Southern Oscillation. *Mon. Wea. Rev.*, **109**, 813–829.

604 Ishii, M., A. Shouji, S. Sugimoto, and T. Matsumoto, 2005: Objective analyses of sea-surface
605 temperature and marine meteorological variables for the 20th century using ICOADS and
606 the Kobe Collection. *Int. J. Climatol.*, **25**, 865–879.

607 Jin, F-F., and B. J. Hoskins, 1995: The direct response to tropical heating in a baroclinic
608 atmosphere. *J. Atmos. Sci.*, **52**, 307–319.

609 JMA, 2021a: Factors behind the heavy snowfall and low temperatures in Japan from mid-
610 December 2020 onward and weather outlook (Available online at:
611 http://ds.data.jma.go.jp/tcc/tcc/news/press_20210115.pdf, accessed 23 February 2022).

612 JMA, 2021b: TCC News No. 64: Summary of the 2020/2021 Asian winter monsoon
613 (Available online at <http://ds.data.jma.go.jp/tcc/tcc/news/tccnews64.pdf>, accessed 23
614 February 2022).

615 Kobayashi, S., Y. Ota, Y. Harada, A. Ebita, M. Moriya, H. Onoda, K. Onogi, H. Kamahori, C.
616 Kobayashi, H. Endo, K. Miyaoka, and K. Takahashi, 2015: The JRA-55 Reanalysis:

617 General specifications and basic characteristics. *J. Meteor. Soc. Japan*, **93**, 5–48.

618 Kodera, K., 1998: Consideration of the origin of the different midlatitude atmospheric
619 responses among El Niño events. *J. Meteor. Soc. Japan*, **76**, 347–361.

620 Koide, H., and K. Kodera, 1999: A SVD analysis between the winter NH 500-hPa height and
621 surface temperature fields. *J. Meteor. Soc. Japan*, **77**, 47–61.

622 Kuramochi, M., H. Ueda, C. Kobayashi, Y. Kamae, and K. Takaya, 2021: Anomalous warm
623 winter 2019/2020 over East Asia associated with trans-basin Indo-Pacific connections.
624 *SOLA*, **17B**, 9–13.

625 Lau, N-C., 1979: The observed structure of tropospheric stationary waves and the local
626 balances of vorticity and heat. *J. Atmos. Sci.*, **36**, 996–1016.

627 Liebmann B., and C. A. Smith, 1996: Description of a complete (interpolated) outgoing
628 longwave radiation dataset. *Bull. Amer. Meteor. Soc.*, **77**, 1275–1277.

629 Madden, R. A., and P. R. Julian, 1972: Description of global-scale circulation cells in the
630 tropics with a 40–50 day period. *J. Atmos. Sci.*, **29**, 1109–1123.

631 Matsuno, T., 1966: Quasi-geostrophic motions in the equatorial area. *J. Meteor. Soc. Japan*,
632 **44**, 25–43.

633 Mori, M., and M. Watanabe, 2008: The growth and triggering mechanisms of the PNA: A
634 MJO-PNA coherence. *J. Meteor. Soc. Japan*, **86**, 213–236.

635 Nishihira, G., and S. Sugimoto, 2022: Severe cold winters in East Asia linked to first winter
636 of La Niña events and in North America linked to second winter. *Geophys. Res. Lett.*, **49**,

637 e2021GL095334, doi:10.1029/2021GL095334.

638 Park, H.-J., and J.-B. Ahn, 2016: Combined effect of the Arctic oscillation and the western
639 Pacific pattern on East Asia winter temperature. *Climate Dyn.*, **46**, 3205–3221.

640 Pavan, V., S. Tibaldi, and Č Branković, 2000: Seasonal prediction of blocking frequency:
641 Results from winter ensemble experiments. *Quart. J. Roy. Meteor. Soc.*, **126**, 2125–2142.

642 Qin, J., and W. A. Robinson, 1993: On the Rossby wave source and the steady linear
643 response to tropical forcing. *J. Atmos. Sci.*, **50**, 1819–1823.

644 Rasmusson, E. M., and K. Mo, 1993: Linkages between 200-mb tropical and extratropical
645 circulation anomalies during the 1986–1989 ENSO cycle. *J. Climate*, **6**, 595–616.

646 Reynolds, R. W., T. M. Smith, C. Liu, D. B. Chelton, K. S. Casey, and M. G. Schlax, 2007:
647 Daily high-resolution-blended analyses for sea surface temperature. *J. Climate*, **20**, 5473–
648 5496.

649 Rivière, G., 2010: Role of Rossby wave breaking in the west Pacific teleconnection.
650 *Geophys. Res. Lett.*, **37**, L11802, doi:10.1029/2010GL043309.

651 Sakai, K., and R. Kawamura, 2009: Remote response of the East Asian winter monsoon to
652 tropical forcing related to El Niño–Southern oscillation. *J. Geophys. Res.*, **114**, D06105,
653 doi:10.1029/2008JD010824.

654 Sardeshmukh, P. D., and B. J. Hoskins, 1988: The generation of global rotational flow by
655 steady idealized tropical divergence. *J. Atmos. Sci.*, **45**, 1228–1251.

656 Sekizawa, S., H. Nakamura, and Y. Kosaka, 2021: Remote influence of the interannual

657 variability of the Australian summer monsoon on wintertime climate in East Asia and the
658 western North Pacific, *J. Climate*, **34**, 9551–9570.

659 Seo, K.-H., and S.-W. Son, 2012: The global atmospheric circulation response to tropical
660 diabatic heating associated with the Madden–Julian oscillation during northern winter. *J.*
661 *Atmos. Sci.*, **69**, 79–96.

662 Seo, K.-H., and H.-J. Lee, 2017: Mechanisms for a PNA-like teleconnection pattern in
663 response to the MJO. *J. Atmos. Sci.*, **74**, 1767–1781.

664 Shiozaki, M., T. Enomoto, and K. Takaya, 2021: Disparate midlatitude responses to the
665 eastern Pacific El Niño. *J. Climate*, **34**, 773–786.

666 Shiozaki, M., and T. Enomoto, 2021: Two types of mid-latitudes responses during La Niña.
667 *SOLA*, **17**, 103–108.

668 Takaya, K., and H. Nakamura, 2001: A formulation of a phase-independent wave-activity flux
669 for stationary and migratory quasigeostrophic eddies on a zonally varying basic flow. *J.*
670 *Atmos. Sci.*, **58**, 608–627.

671 Takaya, K., and H. Nakamura, 2005: Geographical dependence of upper-level blocking
672 formation associated with intraseasonal amplification of the Siberian high. *J. Atmos. Sci.*,
673 **62**, 4441–4449.

674 Takaya, K., and H. Nakamura, 2013: Interannual variability of the East Asian winter monsoon
675 and related modulations of the Planetary waves. *J. Climate*, **26**, 9445–9461.

676 Tanaka, S., K. Nishii, and H. Nakamura, 2016: Vertical structure and energetics of the

677 western Pacific teleconnection pattern. *J. Climate*, **29**, 6597–6616.

678 Trenberth, K. E., 1997: The definition of El Niño. *Bull. Amer. Meteor. Soc.*, **78**, 2771–2777.

679 Trenberth, K. E., G. W. Branstator, D. Karoly, A. Kumar, N. C. Lau, and C. Ropelewski, 1998:
680 Progress during TOGA in understanding and modeling global teleconnections associated
681 with tropical sea surface temperatures. *J. Geophys. Res.*, **103**, 14291–14324.

682 Tseng, K., E. Maloney, and E. A. Barnes, 2020: The consistency of MJO teleconnection
683 patterns on interannual time scales. *J. Climate*, **33**, 3471–3486.

684 Ueda, H., A. Kibe, M. Saitoh, and T. Inoue, 2015: Snowfall variations in Japan and its linkage
685 with tropical forcing. *Int. J. Climatol.*, **35**, 991–998.

686 Wallace, J. M., and D. S. Gutzler, 1981: Teleconnections in the geopotential height field
687 during the Northern Hemisphere winter. *Mon. Wea. Rev.*, **109**, 784–812.

688 Wang, B., R. Wu, and X. Fu, 2000: Pacific–East Asian teleconnection: How does ENSO
689 affect East Asian climate? *J. Climate*, **13**, 1517–1536.

690 Watanabe, M., and M. Kimoto, 2000: Atmosphere-ocean thermal coupling in the North
691 Atlantic: a positive feedback. *Quart. J. Roy. Meteor. Soc.*, **126**, 3343–3369.

692 Wu, G., B. He, Y. Liu, Q. Bao, and R. Ren, 2015a: Location and variation of the summertime
693 upper-troposphere temperature maximum over South Asia. *Climate Dyn.*, **45**, 2757–2774.

694 Wu, G., A. Duan, Y. Liu, J. Mao, R. Ren, Q. Bao, B. He, B. Liu, and W. Hu, 2015b: Tibetan
695 Plateau climate dynamics: recent research progress and outlook. *National Science
696 Review*, **2**, 100–116.

697 Yanai, M., S. Esbensen, and J. H. Chu, 1973: Determination of bulk properties of tropical
698 cloud clusters from large-scale heat and moisture budgets. *J. Atmos. Sci.*, **30**, 611–627.

699 Zheng, J., Q. Liu, C. Wang, and X.-T. Zheng, 2013: Impact of heating anomalies associated
700 with rainfall variations over the Indo-western Pacific on Asian atmospheric circulation in
701 winter. *Climate Dyn.*, **40**, 2023–2033.

702 Zhou, L. T., and R. Wu, 2010: Respective impacts of the East Asian winter monsoon and
703 ENSO on winter rainfall in China. *J. Geophys. Res.*, **115**, D02107,
704 doi:10.1029/2009JD012502.

List of Figures

705

706

707 Fig. 1 (a) Time series of 5-day running mean air temperature anomaly at 850 hPa over East
708 Asia [25° – 45° N, 100° – 140° E] (red and blue shading) and SST indices (blue and orange
709 lines) (unit: $^{\circ}$ C). The indices are defined as SST anomalies averaged as follows: in Niño-
710 3.4 as [5° S– 5° N, 170° E– 120° W]; and in Niño-WP as [0° – 10° N, 130° E– 150° E]. (b)
711 Anomalies of streamfunction (contours; unit: 10^6 m² s⁻¹), air temperature (shading;
712 unit: $^{\circ}$ C), and horizontal wind (vectors; unit: m s⁻¹) at 850 hPa averaged in Period 1
713 (December 13, 2020–January 11, 2021). (c) Same as (b) but for Period 2 (January 23,
714 2021–February 21, 2021). Purple rectangle indicates the East Asia region in this study.

715

716 Fig. 2 (a) Averaged anomalies of streamfunction (contours with an interval of 3.0×10^6 m²
717 s⁻¹) at 250 hPa and OLR (shading; unit: W m⁻²) in Period 1. Gray vectors indicate the
718 wave-activity flux (unit: m² s⁻²) at 250 hPa. (b) Same as (a), but for Period 2. (c) Averaged
719 anomalies of velocity potential (contours; unit: 10^6 m² s⁻¹) and divergent wind (vectors;
720 unit: m s⁻¹) at 200 hPa in Period 1. (d) Same as (c) but for Period 2. Scale for arrows is
721 given on the lower-right side.

722

723 Fig. 3 Time–longitude cross sections of 7-day running mean OLR anomaly averaged over
724 the tropics 10° S– 10° N in the Indo–Pacific region during the winter of 2020/21. The unit is

725 $W m^{-2}$.

726

727 Fig. 4 DJF climatological mean (a) absolute vorticity (shading; unit: $10^{-5} s^{-1}$), zonal wind
728 (white contours; unit: $m s^{-1}$), (b) divergence of wind (shading; unit: $10^{-6} s^{-1}$), and divergent
729 wind (vectors; unit: $m s^{-1}$) at 250 hPa. Scale for arrows is given on the lower-right side.

730

731 Fig. 5 (a) RWS and (b) rotational terms in Eq. (2) based on time-averaged flow at 250 hPa
732 in Period 1 (shading). (c)–(f) Decomposition of RWS into (c) anomalous divergence term
733 (S_1 ; $-\bar{\zeta}D'$), (d) anomalous advection term (S_2 ; $-\mathbf{v}'_{\chi} \cdot \nabla\bar{\zeta}$), (e) climatological divergence
734 term (S_3 ; $-\zeta'\bar{D}$), and (f) climatological advection term (S_4 ; $-\bar{\mathbf{v}}_{\chi} \cdot \nabla\zeta'$) in Eq. (3). Intervals
735 of shading are $0.4 \times 10^{-10} s^{-2}$. Black contours indicate vorticity anomaly averaged in the
736 period (unit: $10^{-5} s^{-1}$).

737

738 Fig. 6 Same as Fig. 5, but for Period 2.

739

740 Fig. 7 (a) Composited deviations of geopotential height (contours; unit: m) at 250 hPa and
741 OLR (shading; unit: $W m^{-2}$) between the 20 strongest positive months and the 21 negative
742 months of the SAJ index. (b) Same as (a), but for the deviations between the 11 strongest
743 positive months and the 9 negative months of the WP-like index which satisfied the criteria
744 of tropical convection (see text for definitions of the indices and details of the criteria).

745 Rectangles indicate regions used for the indices. (c, d) Same as (a, b), respectively, but
746 for geopotential height (contours; unit: m), air temperature (shading; unit: °C), and
747 horizontal wind (vectors; unit: m s^{-1}) at 850 hPa. Black dots indicate statistical significance
748 at the 95% level of the shading quantities. Vectors are plotted only where the zonal or
749 meridional component is statistically significant at the 95% confidence level.

750

751 Fig. 8 (a) (Upper) Composited anomaly of vorticity at 250 hPa in the positive months of the
752 SAJ index. Solid and dashed contours with an interval of $1.0 \times 10^{-5} \text{ s}^{-1}$ indicate positive
753 and negative values, respectively, and zero contours are omitted. Heavy solid and light
754 dashed color rectangles denote the region of the center [20° – 30° N, 90° – 110° E] and
755 upstream node [20° – 30° N, 75° – 95° E] of the anticyclonic eddy, respectively. (Lower) Area-
756 averaged vorticity tendency terms at 250 hPa based on Eq. (4) (unit: 10^{-10} s^{-2}). Heavy
757 and light color bars indicate the center and upstream node of the eddy. (b) Schematic of
758 the vorticity budget of the anticyclonic eddy (AC') over the southeast of the Tibetan
759 Plateau in the upper troposphere associated with the positive phase of the SAJ pattern.
760 Underlines denote the negative value of the term in the vorticity balance. See the text in
761 Sections 4.3 and 6 for the detail.

762

763 Fig. 9 (Upper) Composited anomaly of vorticity at 250 hPa in the positive months of the WP-
764 like index satisfied with the OLR- criteria. Solid and dashed contours with an interval of

765 $1.0 \times 10^{-5} \text{ s}^{-1}$ indicate positive and negative values, respectively, and zero contours are
766 omitted. Rectangle denotes the are-averaged region $[20^{\circ}\text{--}30^{\circ}\text{N}, 130^{\circ}\text{--}160^{\circ}\text{E}]$. (Lower)
767 Area-averaged vorticity tendency terms at 250 hPa based on Eq. (4) (unit: 10^{-10} s^{-2}).

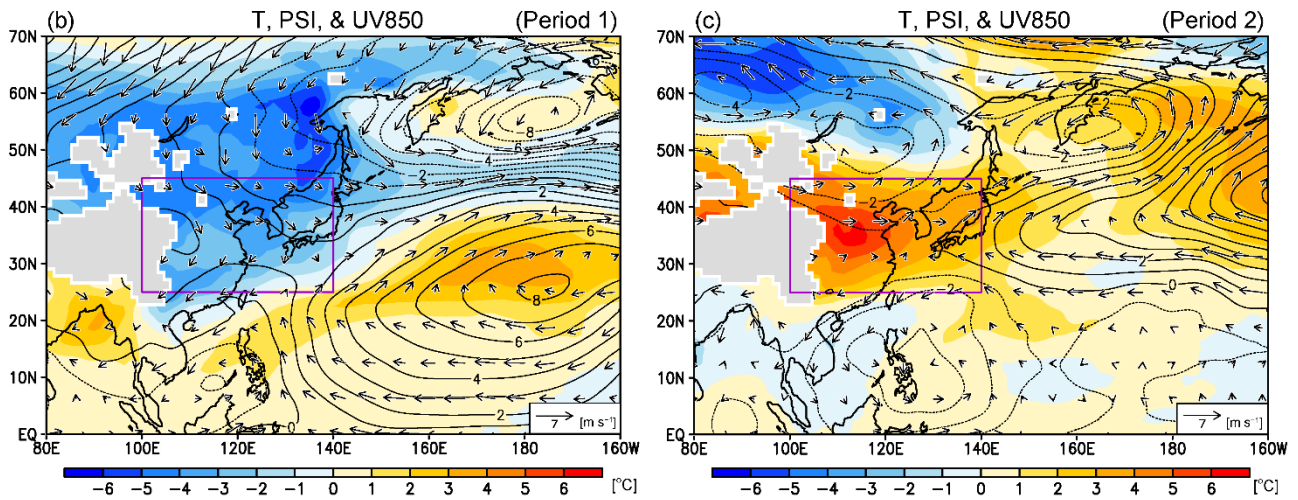
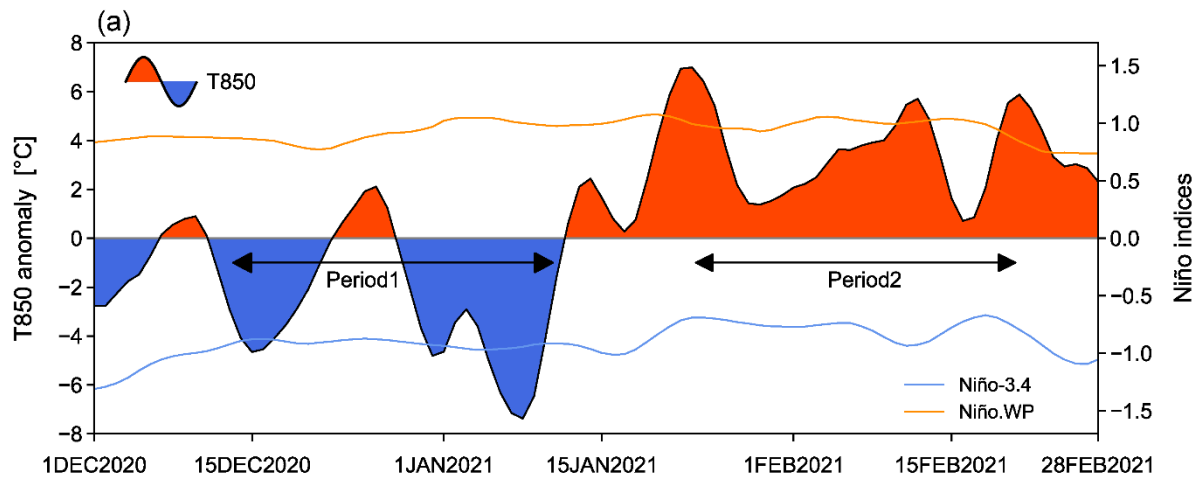
768

769 Fig. 10 Atmospheric response on day 15 in the LBM to the prescribed heating centered at
770 (a) the South China Sea ($8^{\circ}\text{N}, 110^{\circ}\text{E}$) and (b) the Philippine Sea ($10^{\circ}\text{N}, 135^{\circ}\text{E}$). The
771 geopotential height at 250 hPa are plotted (contour intervals: 2.0 m). Purple solid contours
772 indicate prescribed heating ($+0.6 \text{ K day}^{-1}$ and $+0.3 \text{ K day}^{-1}$) at $\sigma = 0.45$. Black dots are
773 the anticyclone center specified as the maximum of the streamfunction at 250 hPa on
774 days 1, 2, 3, 5, 10, and 15 in the LBM. The numbers near the dots denote the days.

775

776 Fig. 11 Upper-tropospheric perturbation associated with the EOF modes of the interannual
777 variation of geopotential height at 250 hPa over Asia $[10^{\circ}\text{S}\text{--}70^{\circ}\text{N}, 10^{\circ}\text{--}180^{\circ}\text{E}]$ from
778 1974/75 to 2020/21. Black contours denote regression coefficients between the
779 streamfunction at 250 hPa and the (a) first and (b) second principal component indices
780 (unit: $10^6 \text{ m}^2 \text{ s}^{-1}$). Red and blue shading denote positive and negative correlation
781 exceeding the 90% confidence level, respectively. (c, d) Same as (a, b), respectively, but
782 for OLR (shading; unit: W m^{-2}). Black dots indicate statistical significance at the 90% level.
783 The signs of second mode were adjusted to the opposite.

784



785

786

787 Fig. 1 (a) Time series of 5-day running mean air temperature anomaly at 850 hPa over East

788 Asia [25° – 45° N, 100° – 140° E] (red and blue shading) and SST indices (blue and orange

789 lines) (unit: $^{\circ}$ C). The indices are defined as SST anomalies averaged as follows: in Niño-

790 3.4 as [5° S– 5° N, 170° E– 120° W]; and in Niño-WP as [0° – 10° N, 130° E– 150° E]. (b)

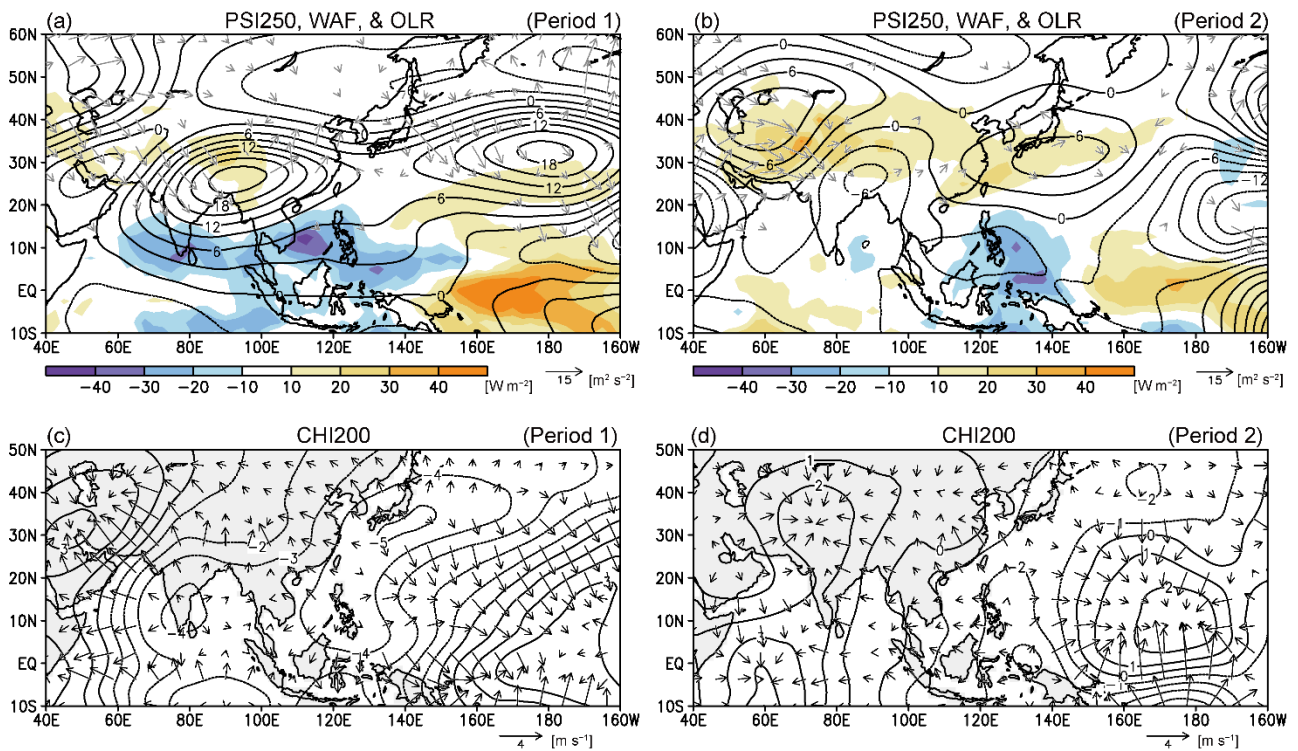
791 Anomalies of streamfunction (contours; unit: 10^6 m^2 s^{-1}), air temperature (shading;

792 unit: $^{\circ}$ C), and horizontal wind (vectors; unit: m s^{-1}) at 850 hPa averaged in Period 1

793 (December 13, 2020–January 11, 2021). (c) Same as (b) but for Period 2 (January 23,

794 2021–February 21, 2021). Purple rectangle indicates the East Asia region in this study.

795



796

797

798 Fig. 2 (a) Averaged anomalies of streamfunction (contours with an interval of $3.0 \times 10^6 \text{ m}^2$

799 s^{-1}) at 250 hPa and OLR (shading; unit: W m^{-2}) in Period 1. Gray vectors indicate the

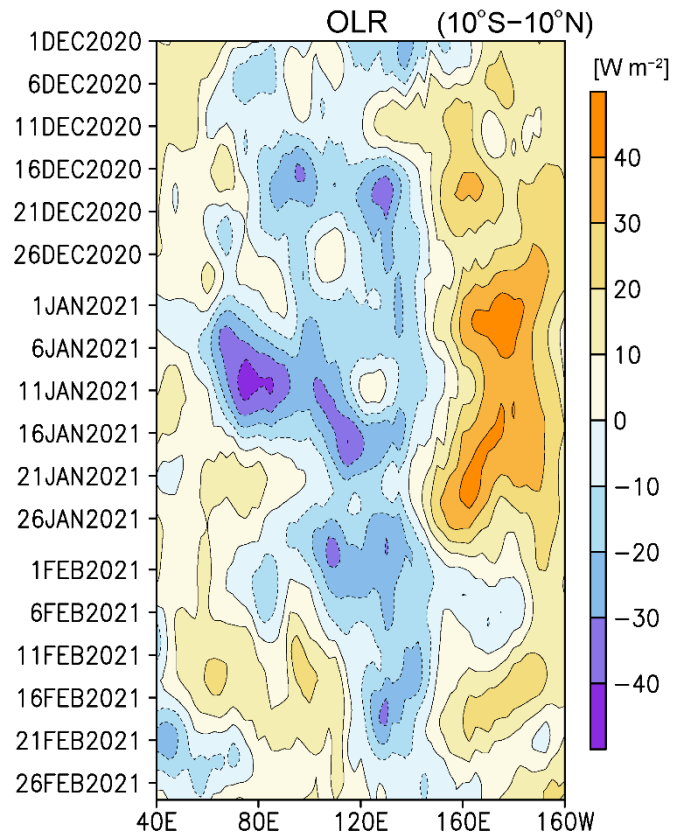
800 wave-activity flux (unit: $\text{m}^2 \text{ s}^{-2}$) at 250 hPa. (b) Same as (a), but for Period 2. (c) Averaged

801 anomalies of velocity potential (contours; unit: $10^6 \text{ m}^2 \text{ s}^{-1}$) and divergent wind (vectors;

802 unit: m s^{-1}) at 200 hPa in Period 1. (d) Same as (c) but for Period 2. Scale for arrows is

803 given on the lower-right side.

804



805

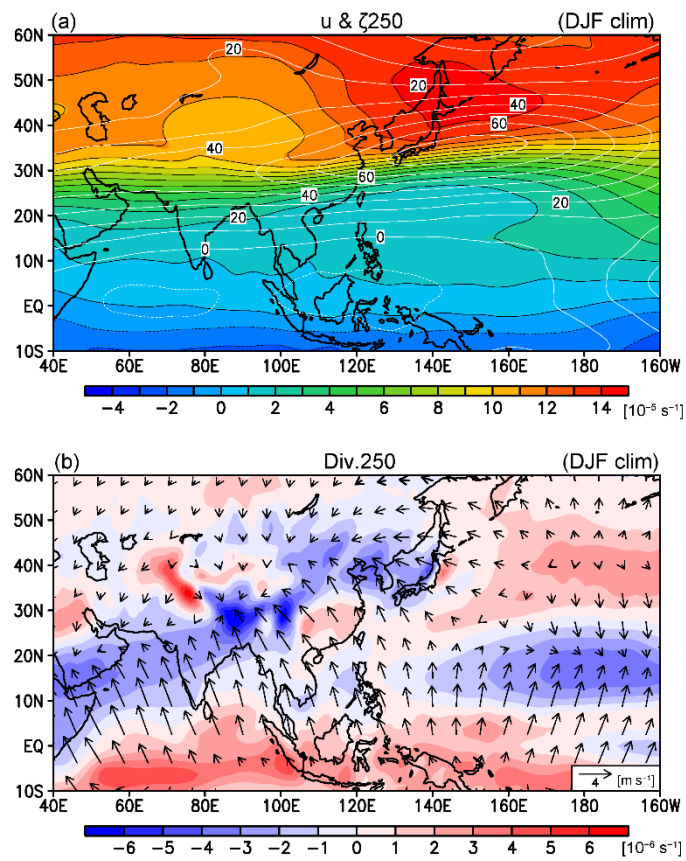
806

807 Fig. 3 Time–longitude cross sections of 7-day running mean OLR anomaly averaged over

808 the tropics 10°S–10°N in the Indo–Pacific region during the winter of 2020/21. The unit is

809 W m⁻².

810



811

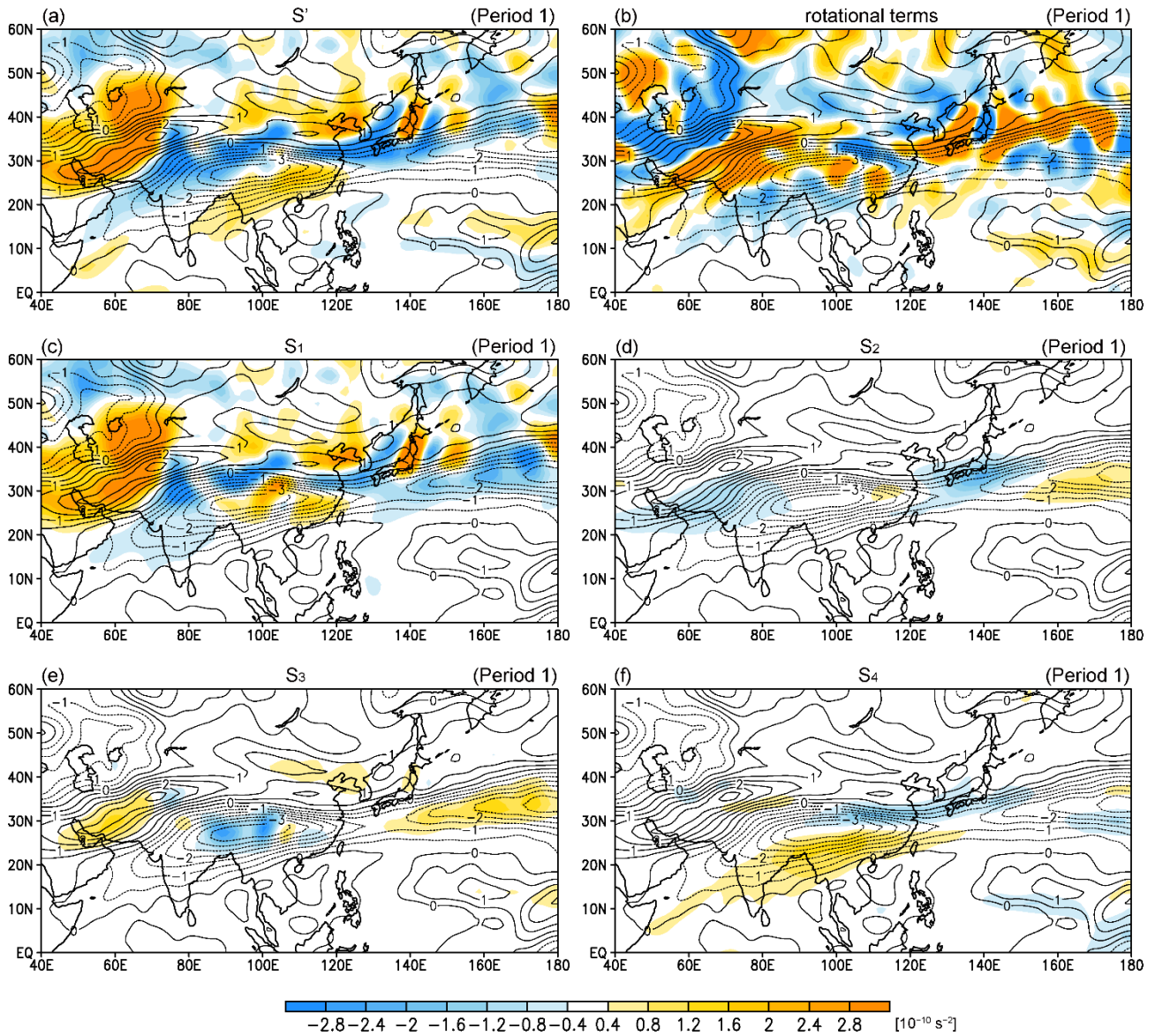
812

813 Fig. 4 DJF climatological mean (a) absolute vorticity (shading; unit: 10^{-5} s^{-1}), zonal wind

814 (white contours; unit: m s^{-1}), (b) divergence of wind (shading; unit: 10^{-6} s^{-1}), and divergent

815 wind (vectors; unit: m s^{-1}) at 250 hPa. Scale for arrows is given on the lower-right side.

816



817

818

819 Fig. 5 (a) RWS and (b) rotational terms in Eq. (2) based on time-averaged flow at 250 hPa

820 in Period 1 (shading). (c)–(f) Decomposition of RWS into (c) anomalous divergence term

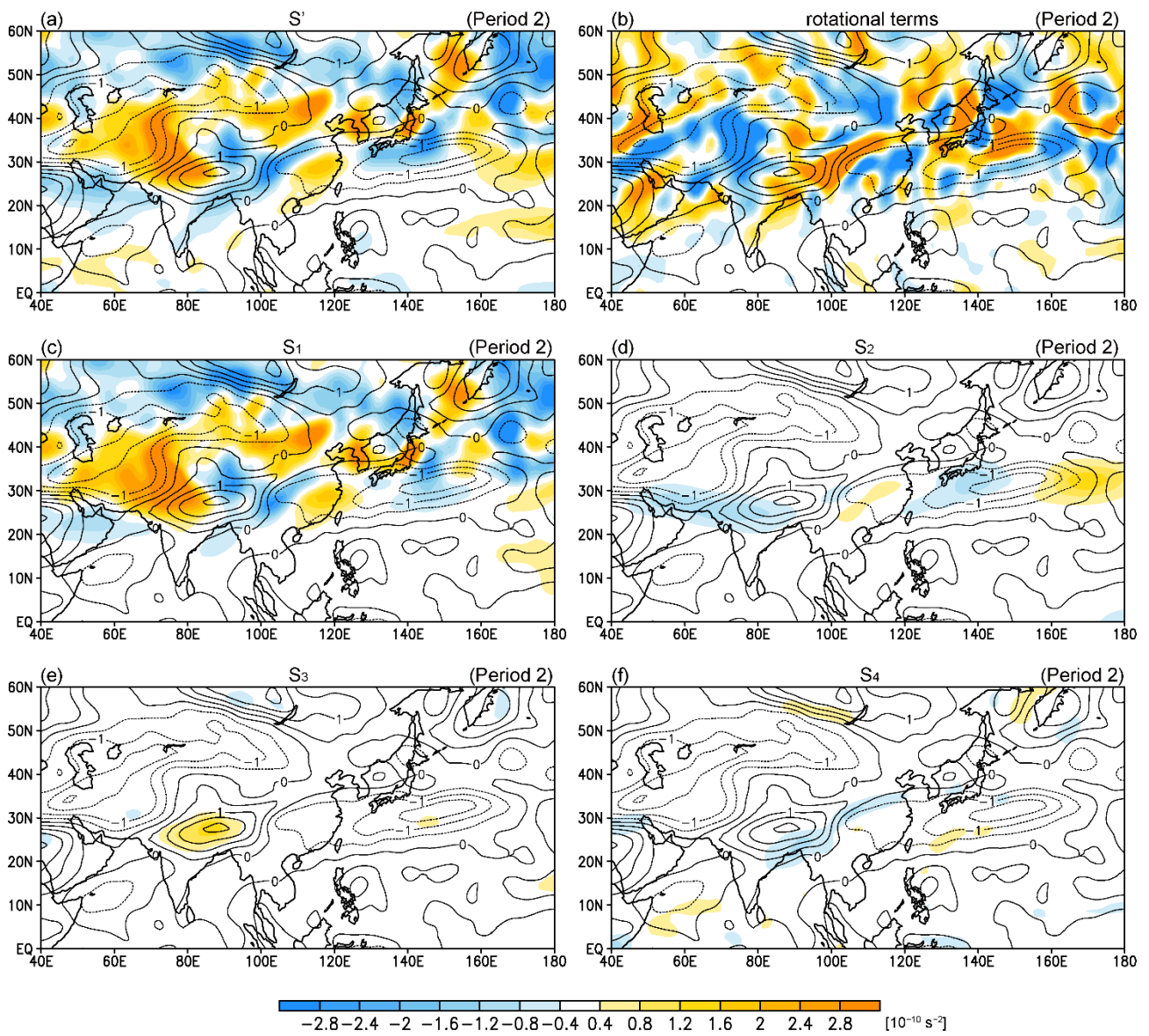
821 (S_1 ; $-\bar{\zeta}'D'$), (d) anomalous advection term (S_2 ; $-\mathbf{v}'_{\chi} \cdot \nabla \bar{\zeta}$), (e) climatological divergence

822 term (S_3 ; $-\zeta'\bar{D}$), and (f) climatological advection term (S_4 ; $-\bar{\mathbf{v}}_{\chi} \cdot \nabla \zeta'$) in Eq. (3). Intervals

823 of shading are $0.4 \times 10^{-10} \text{ s}^{-2}$. Black contours indicate vorticity anomaly averaged in the

824 period (unit: 10^{-5} s^{-1}).

825

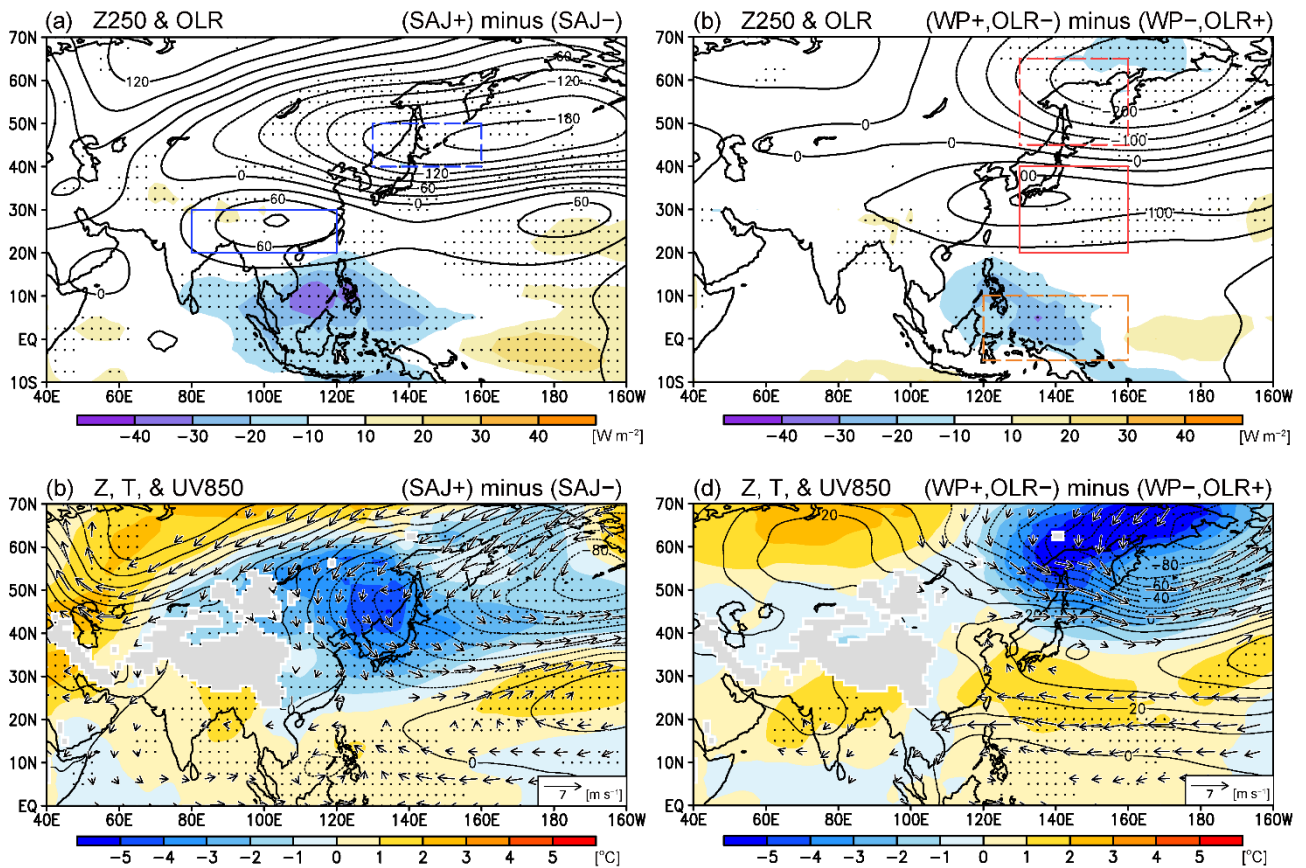


826

827

828 Fig. 6 Same as Fig. 5, but for Period 2.

829



830

831 Fig. 7 (a) Composited deviations of geopotential height (contours; unit: m) at 250 hPa and

832 OLR (shading; unit: $W m^{-2}$) between the 20 strongest positive months and the 21 negative

833 months of the SAJ index. (b) Same as (a), but for the deviations between the 11 strongest

834 positive months and the 9 negative months of the WP-like index which satisfied the criteria

835 of tropical convection (see text for definitions of the indices and details of the criteria).

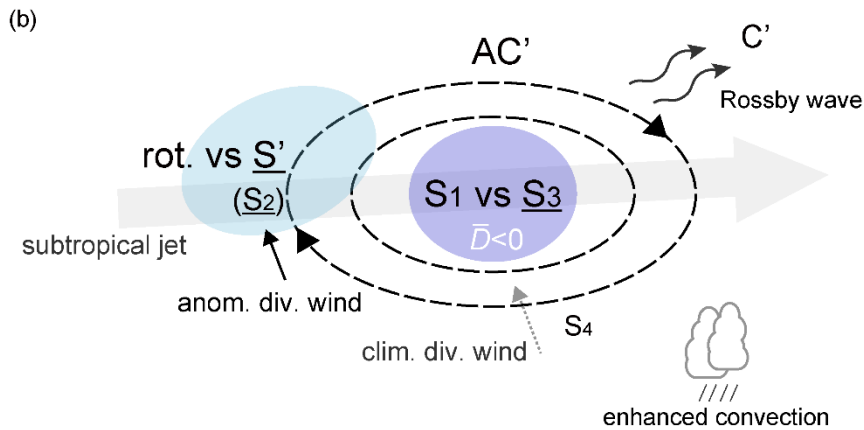
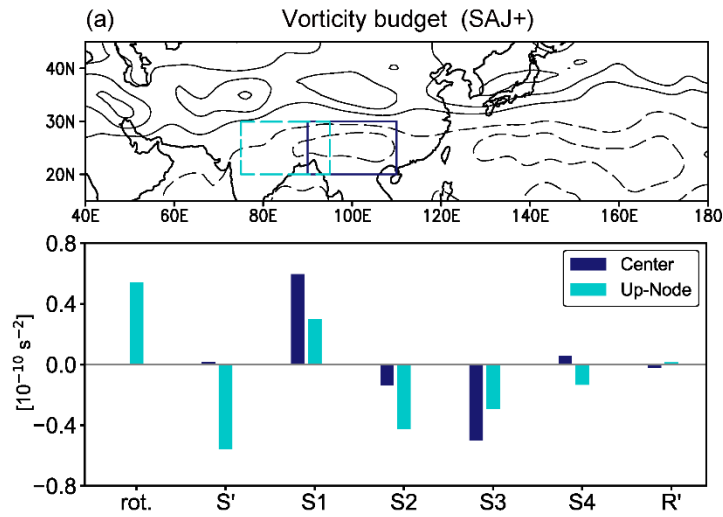
836 Rectangles indicate regions used for the indices. (c, d) Same as (a, b), respectively,

837 for geopotential height (contours; unit: m), air temperature (shading; unit: $^{\circ}C$), and

838 horizontal wind (vectors; unit: $m s^{-1}$) at 850 hPa. Black dots indicate statistical significance

839 at the 95% level of the shading quantities. Vectors are plotted only where the zonal or

840 meridional component is statistically significant at the 95% confidence level.



841

842 Fig. 8 (a) (Upper) Composited anomaly of vorticity at 250 hPa in the positive months of the

843 SAJ index. Solid and dashed contours with an interval of $1.0 \times 10^{-5} \text{ s}^{-1}$ indicate positive

844 and negative values, respectively, and zero contours are omitted. Heavy solid and light

845 dashed color rectangles denote the region of the center [20° – 30° N, 90° – 110° E] and

846 upstream node [20° – 30° N, 75° – 95° E] of the anticyclonic eddy, respectively. (Lower) Area-

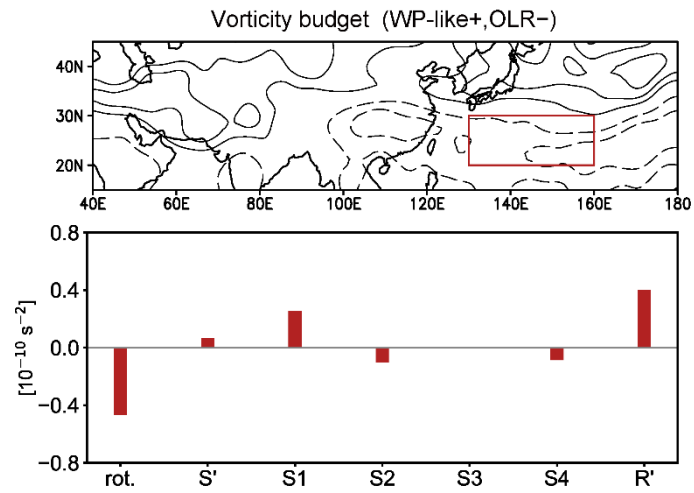
847 averaged vorticity tendency terms at 250 hPa based on Eq. (4) (unit: 10^{-10} s^{-2}). Heavy

848 and light color bars indicate the center and upstream node of the eddy. (b) Schematic of

849 the vorticity budget of the anticyclonic eddy (AC') over the southeast of the Tibetan

850 Plateau in the upper troposphere associated with the positive phase of the SAJ pattern.

851 Underlines denote the negative value of the term in the vorticity balance. See the text in
852 Sections 4.3 and 6 for the detail.



853

854 Fig. 9 (Upper) Composited anomaly of vorticity at 250 hPa in the positive months of the WP-

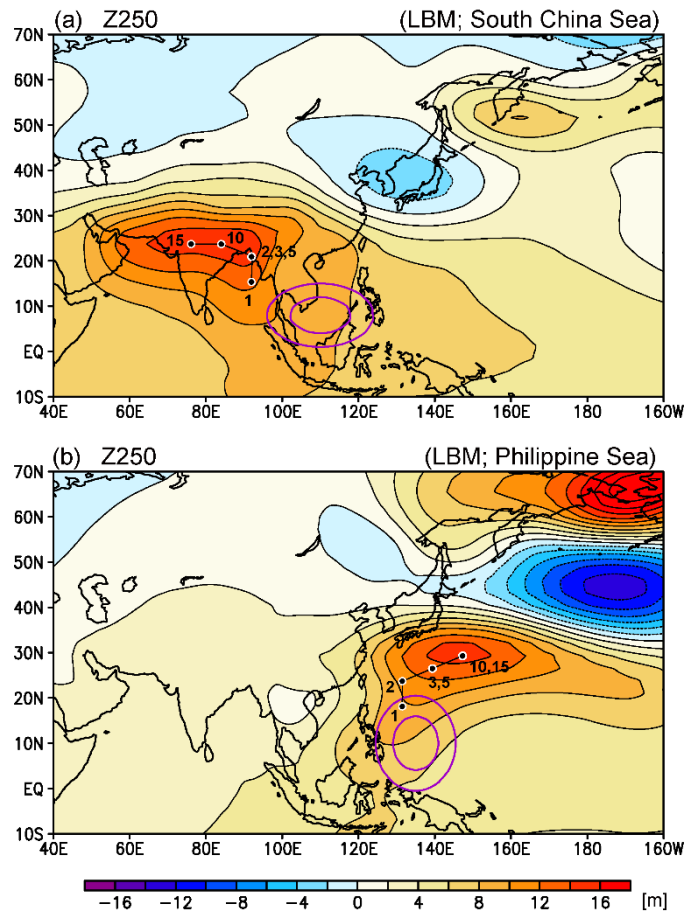
855 like index satisfied with the OLR- criteria. Solid and dashed contours with an interval of

856 $1.0 \times 10^{-5} \text{ s}^{-1}$ indicate positive and negative values, respectively, and zero contours are

857 omitted. Rectangle denotes the area-averaged region $[20^{\circ}\text{--}30^{\circ}\text{N}, 130^{\circ}\text{--}160^{\circ}\text{E}]$. (Lower)

858 Area-averaged vorticity tendency terms at 250 hPa based on Eq. (4) (unit: 10^{-10} s^{-2}).

859



860

861

862 Fig. 10 Atmospheric response on day 15 in the LBM to the prescribed heating centered at

863 (a) the South China Sea (8°N, 110°E) and (b) the Philippine Sea (10°N, 135°E). The

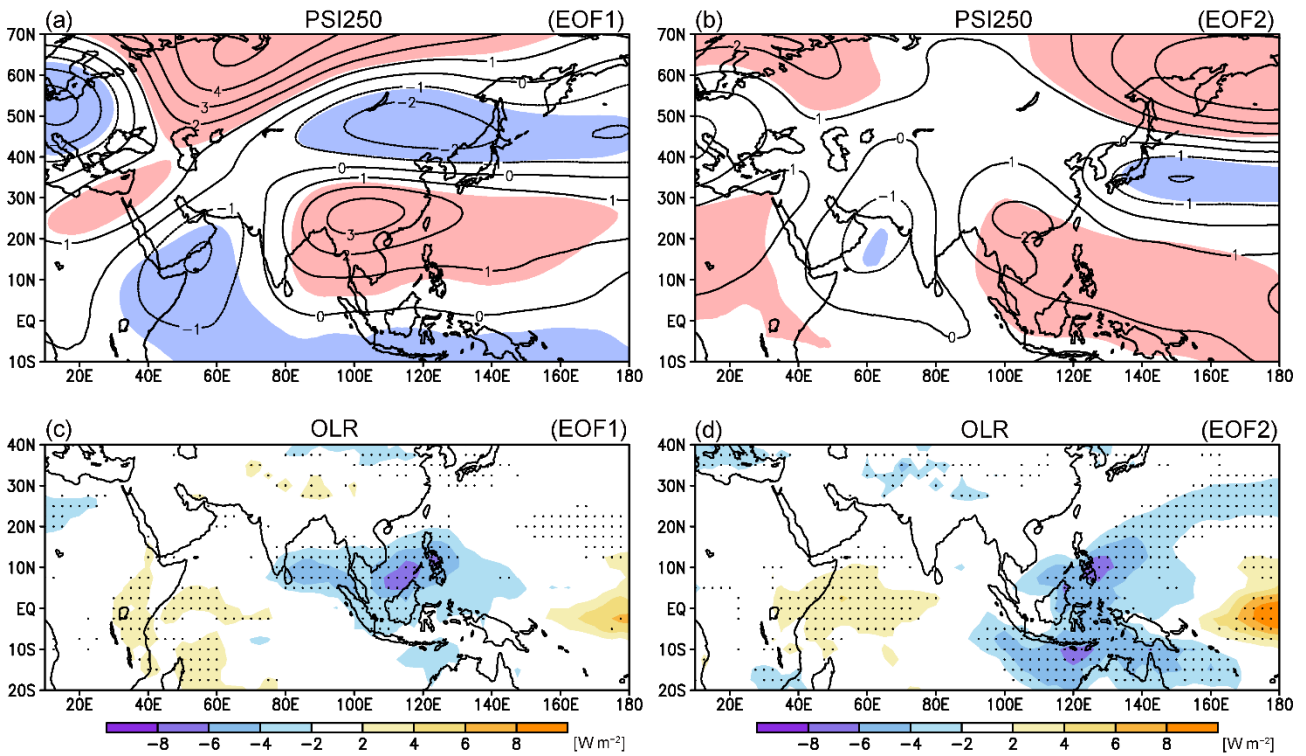
864 geopotential height at 250 hPa are plotted (contour intervals: 2.0 m). Purple solid contours

865 indicate prescribed heating ($+0.6 \text{ K day}^{-1}$ and $+0.3 \text{ K day}^{-1}$) at $\sigma = 0.45$. Black dots are

866 the anticyclone center specified as the maximum of the streamfunction at 250 hPa on

867 days 1, 2, 3, 5, 10, and 15 in the LBM. The numbers near the dots denote the days.

868



870

871

872 Fig. 11 Upper-tropospheric perturbation associated with the EOF modes of the interannual
 873 variation of geopotential height at 250 hPa over Asia [$10^{\circ}S-70^{\circ}N$, $10^{\circ}-180^{\circ}E$] from
 874 1974/75 to 2020/21. Black contours denote regression coefficients between the
 875 streamfunction at 250 hPa and the (a) first and (b) second principal component indices
 876 (unit: $10^6 m^2 s^{-1}$). Red and blue shading denote positive and negative correlation
 877 exceeding the 90% confidence level, respectively. (c, d) Same as (a, b), respectively, but
 878 for OLR (shading; unit: $W m^{-2}$). Black dots indicate statistical significance at the 90% level.
 879 The signs of second mode were adjusted to the opposite.

880

List of Tables

881
882
883
884
885
886
887
888
889
890
891
892
893
894
895
896
897

Table 1 The months that the SAJ and WP-like indices exceeded +1 (-1) standard deviation. The 20 positive SAJ months and 21 negative SAJ months were used for the composite analysis of the SAJ pattern. The 11 positive WP-like with OLR- months and 9 negative WP-like with OLR+ months were used for the composite analysis of WP-like pattern accompanied by corresponded anomalous convection. See text for definitions of the indices and details of the criteria.

Table 2 Correlation coefficients between the teleconnection indices (the SAJ pattern and the WP-like pattern) and the ENSO indices (Niño-3.4 and Niño-WP) based on monthly mean data (n = 141 months). The values in parentheses are based on DJF mean (n = 47 winters). Single and double asterisks denote the 95% and 99.9% confidence levels, respectively.

898 Table 1 The months that the SAJ and WP-like indices exceeded +1 (-1) standard deviation.
 899 The 20 positive SAJ months and 21 negative SAJ months are used for the composite
 900 analysis of the SAJ pattern. The 11 positive WP-like with OLR- months and 9 negative
 901 WP-like with OLR+ months were used for the composite analysis of WP-like pattern
 902 accompanied by corresponded anomalous convection. See text for definitions of the
 903 indices and details of the criteria.

	Positive		Negative	
SAJ	Feb 1977, Feb 1978, Jan 1981, Feb 1984, Jan 1986, Feb 1988, Feb 1999, Feb 2000, Dec 2000, Jan 2001, Feb 2001, Dec 2005, Jan 2006, Dec 2011, Feb 2012, Feb 2013, Dec 2014, Dec 2017, Dec 2020, and Jan 2021 (n = 20)		Feb 1976, Feb 1979, Dec 1979, Dec 1986, Jan 1989, Feb 1989, Dec 1989, Feb 1990, Dec 1990, Dec 1991, Jan 1992, Dec 1992, Jan 1993, Jan 1997, Dec 1997, Jan 2000, Feb 2007, Feb 2011, Feb 2014, Feb 2015, and Jan 2020 (n = 21)	
WP-like	OLR- Dec 1974, Jan 1989, Dec 1998, Feb 1999, Feb 2001, Feb 2006, Jan 2008, Feb 2009, Feb 2012, Feb 2013, and Jan 2021 (n = 11)	OLR+ Dec 1982, Dec 1987, Jan 1988, Dec 2006, Jan 2016, Feb 2016, Dec 2018, Feb 2019, Dec 2019, and Dec 2020 (n = 10)	OLR- Dec 1980, Feb 1982, Dec 1983, Feb 1986, Dec 1989, Jan 1991, Dec 1992, Dec 1995, Jan 1997, Dec 2005, Dec 2013, Feb 2014, and Feb 2015 (n = 13)	OLR+ Feb 1975, Feb 1979, Jan 1984, Feb 1985, Feb 1994, Feb 1995, Jan 2004, Dec 2009, and Dec 2010 (n = 9)

904

905 Table 2 Correlation coefficients between the teleconnection indices (the SAJ pattern and
906 the WP-like pattern) and the ENSO indices (Niño-3.4 and Niño-WP) based on monthly
907 mean data (n = 141 months). The values in parentheses are based on DJF mean (n =
908 47 winters). Single and double asterisks denote the 95% and 99.9% confidence levels,
909 respectively.

910
911

	Niño-3.4	Niño-WP
SAJ	-0.25* (-0.38*)	0.27** (0.51**)
WP-like	0.10 (0.13)	0.11 (0.16)

912
913